Shape-morphing structures based on perforated kirigami

Yunlan Zhang[1,4], Jingyi Yang[1], Mingchao Liu[2,*] and Dominic Vella[3]

[1] *Department of Engineering Science, University of Oxford, Parks Rd, Oxford, OX1 3JP, UK*
[2] *School of Mechanical and Aerospace Engineering, Nanyang Technological University, Singapore 639798, Republic of Singapore*
[3] *Mathematical Institute, University of Oxford, Woodstock Rd, Oxford, OX2 6GG, UK*
[4] *Department of Civil, Architectural and Environmental Engineering, University of Texas at Austin, Austin, TX 78712, United States of America*

Abstract

Shape-morphing structures, which are able to change their shapes from one state to another, are important in a wide range of engineering applications. A popular scenario is morphing from an initial two-dimensional (2D) shape that is flat to a three-dimensional (3D) target shape. One of the exciting manufacturing paradigms is transforming flat 2D sheets with prescribed cuts (i.e. kirigami) into 3D structures. By employing the formalism of the tapered elastica equation, we develop an inverse design framework to predict the shape of the 2D cut pattern that would generate a desired axisymmetric 3D shape. Our previous work has shown that tessellated 3D structures can be achieved by designing both the width and thickness of the cut 2D sheet to have particular tapered designs. However, the fabrication of a sample with variable thickness can be challenging and limits the materials that can be used. Here we propose a new strategy — changing the local bending stiffness by adding small pores, or perforations, within the structure to give it a varying porosity but maintaining a constant thickness. We refer to this strategy as 'perforated kirigami' and show how the porosity function can be calculated from a theoretical model. The porosity distribution can easily be realized by laser cutting and modifies the bending stiffness of the sheet to yield a desired elastic deformation upon buckling. To verify our theoretical approach, we conduct finite element simulations and physical experiments. We also examine the load-bearing capacity of morphed structures via indentation tests in both FEM simulations and experiments. As an example, the relationship between the measured geometric rigidity of morphed half-ellipsoids and their aspect ratio is investigated in details.

Keywords: Shape-morphing, Inverse design, Perforated kirigami, Geometric rigidity

1. Introduction

Structures that can adapt to different environments and complete various tasks by changing shapes from one state to another are referred to as shape-morphing structures (Oliver et al., 2016). Shape-morphing structures exist extensively as biological organisms in nature (Huang et al., 2018). They are also an emerging class of advanced structures with engineering applications, including flexible electronics (Wang et al., 2019), microfluidics (Wang et al., 2022), soft robotics (Lum et al.,

---

Corresponding Author: mingchao.liu@ntu.edu.sg (M.L.)

2016; Liu et al., 2021a; Wang et al., 2021), deployable space structures (McCue et al., 2021) and aircraft drag control systems (Sofla et al., 2010; Li et al., 2018), etc. Many mechanisms have been explored to achieve shape morphing in recent years, including pneumatic inflation (Siéfert et al., 2019), thermal expansion (Boley et al., 2019; Zou et al., 2022), chemical swelling (Nojoomi et al., 2018) and solvent diffusion (Yiming et al., 2020; Tao et al., 2021), as well as magnetic (Nguyen et al., 2012; Wang et al., 2020; Bastola and Hossain, 2021; Tang et al., 2021) and mechanical loading (Liu et al., 2020; Meng et al., 2022).

Among many engineering applications, morphing from a flat two-dimensional (2D) sheet into a three-dimensional (3D) structure with particular curvature distribution is one of the most common scenarios and has attracted much attention (van Manen et al., 2018; Nojoomi et al., 2021). However, a significant challenge needs to be conquered first: to prevent the geometrical incompatibility between curved and flat surfaces that Gauss *Theorema Egregium* depicts, i.e. that deformations that preserve length or area (isometries) cannot change the Gaussian curvature of a surface (Gauss, 1828). Creating localized stretching or expanding materials is one possible strategy. It can be achieved by either applying multifarious external physical effects (pressure, heat, and light) to actuate the local expansion or by using chemical stimuli to the material with elaborate micro-structures (Nojoomi et al., 2018; Siéfert et al., 2019; Boley et al., 2019; Liu et al., 2021b). Nevertheless, since thin materials resist changes of length significantly, these approaches all depend on unconventional responsive materials and/or complex manufacturing techniques (Piedade, 2019) to generate high stress/strain concentration at the areas that stretch locally (Vella, 2019).

Instead of locally stretching materials, another strategy is to buffer the geometric incompatibility by removing materials locally, i.e. making cuts at specific positions in a material, known as kirigami (Neville et al., 2016). By programming the cut pattern of kirigami, 3D shapes with different Gaussian curvatures can be generated (Callens and Zadpoor, 2018; Choi et al., 2019). It should be noted that the curvature here referred to is Apparent Gaussian Curvature (AGC), which means that, even though the 3D structure has distributed curvature at a global level, the local elements remain largely planar (Liu et al., 2020). Kirigami-based methods have shown potential for creating 3D structures with the ability of shape reconfiguration (Abdullah et al., 2020) and functional applications (Tang et al., 2017; Yang et al., 2021). In particular, they have been broadly adopted for fabricating inorganic flexible electronic devices with complex 3D shapes, since these methods avoid significant strain (Zhang et al., 2017). Using a design database of kirigami-based morphing structures and devices has become ubiquitous to achieve shape morphing from 2D patterns into 3D structures (Xu et al., 2015). On the contrary, how to design a kirigami 2D sheet that can morph into a given target profile had not been well-explored until analytical inverse design strategies were proposed recently (Liu et al., 2020; Fan et al., 2020).

The inverse design framework developed by Liu et al. (2020) is based on the theory of the tapered elastica (Lee et al., 1993). More specifically, we considered an axisymmetric 3D structure as a target that can be formed from a flat 2D sheet with a tailored cut pattern by subjecting the sheet to a mechanical load. From a mechanics point of view, the 2D cut sheet can be viewed as multiple tapered elastic strips connected at one end to form the central hub. Since the tapered elastica theory can describe the deformation of each strip, we can therefore derive an explicit equation that correlates the shape of the 2D cut pattern (i.e. the width and thickness distributions of each elastic strip) and the curvature of the 3D target structure. We also demonstrated the feasibility of this inverse design framework by showing several typical examples. Implementing the framework of Liu et al. (2020) to create tessellated morphing structures requires fabricating customized flat cut sheets

with tapering of both the width and thickness. Although additive manufacturing technologies, such as 3D printing, allow the manufacture of such customized sheets (Isa and Lazoglu, 2019), this approach is only readily adopted for certain materials — it is not appropriate for others, particularly brittle, crystalline or two-dimensional materials. In addition, it is challenging to precisely control the thickness of preformed flat sheets (Adnan et al., 2017). Therefore, other strategies should be sought that can more readily be implemented for such materials.

Looking into the underlying morphing mechanism, we can realize that the fundamental effect of changing the width or thickness of the kirigami sheet is to tune the local bending stiffness (Lee et al., 1993). Inspired by recent investigations on the bending behaviour of perforated sheets (Pezzulla et al., 2020; Shrimali et al., 2021), we now propose an alternative strategy to tailor the local bending stiffness – introducing distributed small pores (or perforations) into the kirigami sheet, which is referred to as 'perforated kirigami. These pores can be easily introduced by, for example, laser cutting and micro-fabrication techniques (Pezzulla et al., 2020) and modify the bending stiffness of the beam in a similar manner to thickness variations. Together with the geometrical constraint of tessellation (Liu et al., 2020), we present a new paradigm of inverse design of shape-morphing structures in this work and demonstrate it with a series of examples. We also move beyond the simple design problem considered by Liu et al. (2020) to consider the structural stability of the resulting shape: while a tesselated 3D shape may resemble a standard shell, we consider their load-bearing capacity. This is an important consideration since most shape-morphing structures will be required to withstand the action of external loads in applications from aircraft wing, to automobile structures and space or ground infrastructures (Sofla et al., 2010; Daynes and Weaver, 2013; Kormaníková et al., 2017). We therefore examine the load-bearing capacity of the shape-morphing structures generated using this 'perforated kirigami' under indentation tests; in particular, by combining experiments and FEM simulations, we find that these structures have an unusual geometry-dependent rigidity in comparison to continuous shells.

2. Theoretical Model

Our previous work developed a theoretical framework based on the tapered elastica theory for the inverse design of shape-morphing problems (Liu et al., 2020). The key idea is to control its local mechanical properties (namely the bending stiffness) by varying the geometry (i.e. width and/or thickness) of the flat sheet. Since changing the thickness of a thin sheet is generally not easy to achieve, in this work we modify it, achieving the same ultimate effect through variations of the porosity (or the pore volume fraction) combined with tailoring of the width.

To implement the inverse design strategy of shape-morphing by making cuts in a porous sheet, the first step is to correlate the bending stiffness of the porous structure and its micro-structure. The exact expression of the effective bending stiffness of a porous sheet is complex, and depends not only on the overall porosity but also on the spatial distribution and shape of the pores (Shrimali et al., 2021). Here, to simplify the problem, we only focus on the local bending behaviour of the porous sheet. We define the pore volume fraction in a local area with width, h, where pores are located (see the zoom-in in fig. 1(a), marked by yellow box) as the local porosity, $\varphi(s)$, which varies with the arc length, s. Following this definition, the local bending stiffness of a porous strip of length L with non-uniform moment of inertia, $I(s)$, and distributed local porosity, $\varphi(s)$, can be written as

$$B(s) = E_0 \cdot I(s) \cdot [1 - \varphi(s)], \tag{1}$$

3

E_0 is the Young's modulus of the strip, which is a constant. (Here, we focus exclusively on changes to $I(s)$ achieved by varying the width, $w(s)$, keeping the thickness uniform, t_0; we therefore have $I(s) = w(s) \cdot t_0^3/12$ but have left the general expression for completeness.)

Note that the 'local porosity', $\varphi(s)$, in (1) is different from the global porosity, which we denote ϕ and measures the overall volume fraction of pores. In this way, it is possible to tune the global porosity by changing the width of the local area, h, whilst maintaining the same distribution of the local porosity. This advantage is important for customizing the load-bearing capacity of the morphed structures, which will be discussed further in Section 4.

As shown in fig. 1(a), we consider an elastic porous strip subject to horizontal and vertical forces, H_0 and V_0, at its two ends, respectively. Recalling the tapered *elastica* equation (Stuart, 2000; Liu et al., 2020), we write the intrinsic equation for the shape, $\theta(s)$, as

$$-\frac{\mathrm{d}}{\mathrm{d}s}\left[B(s) \cdot \frac{\mathrm{d}\theta(s)}{\mathrm{d}s}\right] = w_0\left[H_0 \sin\theta(s) + V_0 \cos\theta(s)\right]. \tag{2}$$

This is to be solved together with appropriate boundary conditions at both edges, e.g. the clamped condition

$$\theta(0) = \theta(L) = 0, \tag{3}$$

and the geometric constraints arising from the inextensibility, i.e. as shown in fig. 1(a), the beam accommodates a fixed amount of compression, ΔL, which corresponds to

$$\int_0^L \cos\theta(s)\,\mathrm{d}s = L - \Delta L = L(1 - \tilde{\Delta}), \tag{4}$$

where $\tilde{\Delta} = \Delta L/L$.

The complete shape of the buckled elastica, $[\hat{x}(s), \hat{z}(s)]$, may be determined from the intrinsic equation $\theta(s)$ by solving the geometrical relationships

$$\frac{\mathrm{d}\hat{x}}{\mathrm{d}s} = \cos\theta, \quad \frac{\mathrm{d}\hat{z}}{\mathrm{d}s} = \sin\theta. \tag{5}$$

Following Liu et al. (2020), we non-dimensionalize the problem by letting $(\xi, x, z) = (s, \hat{x}, \hat{z})/L$ and $\omega(\xi) = w(s)/w_0$ (where w_0 is the value of the width at $s = 0$); using eqs. (1) and (5), the tapered elastica equation (2) becomes

$$\frac{\mathrm{d}}{\mathrm{d}\xi}\left\{\omega(\xi) \cdot [1 - \varphi(\xi)] \cdot \frac{\mathrm{d}\theta}{\mathrm{d}\xi}\right\} = -\tilde{H}\frac{\mathrm{d}z}{\mathrm{d}\xi} - \tilde{V}\frac{\mathrm{d}x}{\mathrm{d}\xi}, \tag{6}$$

where $\tilde{H} = \left[(w_0L^2)/(E_0I_0)\right] \cdot H_0$ and $\tilde{V} = \left[(w_0L^2)/(E_0I_0)\right] \cdot V_0$ are the dimensionless forces and $I_0 = w_0t_0^3/12$. In addition, both the boundary condition (3) and the geometric constraint (4) are non-dimensionalized correspondingly.

Equation (6) may be referred to as the porous tapered elastica equation but it is worth noting that the main difference between this equation (6) and eq. (8) of Liu et al. (2020) is simply the replacement of $T(\xi)^3$ by $[1 - \varphi(\xi)]$: variations in thickness are replaced by variations of the local solid fraction. Before moving to present the inverse design framework, we first validate this variant of the tapered elastica equation.

According to eq. (6), we might expect to observe deformed shapes with different curvatures simply by controlling the distribution of the local porosity of strips. As a validation, we perform

4

finite element method (FEM) simulations to examine the deformation of three elastic strips with different local porosity distributions but the same thickness and width, as shown in fig. 1(b) (from (i) to (iii) corresponding to $\varphi_0/\varphi_1 = 10$, 1 and 0.1), with clamped boundary conditions at both ends. The deformed shapes of three strips obtained from FEM simulations are shown in fig. 1(c). Given the difficulties of cutting small pores in a narrow strip, we also check the cases with the same local porosity distribution but replacing a row of small pores by a single narrow rectangular slot (with the same pore value ratio in the local area as marked by yellow box in fig. 1(a)). The corresponding deformed shapes obtained from FEM simulations are given in fig. 1(d). The quantitative comparison of the deformed profiles between FEM simulations and theoretical predictions is presented in fig. 1(e), where the symbols on the left- and right-hand side correspond to the shapes in figs. 1(c) and (d), respectively.

As expected, controlling the distribution of the local porosity of 2D strips with uniform thickness and width leads to different deformed shapes upon buckling. More specifically, compare the shape of the uniform strip (either without pores, see fig. 1(c)-(ii), or with uniform local porosity, see fig. 1(d)-(v), with profiles represented in (e) by green curves), with a strip of larger local porosity at the edges, which exhibits a fatter deformed shape, see figs. 1(c)-(i) and (d)-(iv) and the red curve in (e); while the larger local porosity in the centre of the strip with lead to slimmer deformed shape, see figs. 1(c)-(iii) and (d)-(vi) and the blue curve in (e). According to eq. (1), it is natural to understand that the large local porosity will induce sharp curvature because the local bending stiffness is weakened when more material is removed locally. Now, we move on to consider how a desired 3D tessellated shape can be inversely designed by choosing an appropriate bending stiffness of each strip within the perforated kirigami, which in turn can be chosen by tapering the width and making pores to match the desired distribution of the local porosity.

3. Inverse Design of Tessellated 3D Structures

3.1. Theoretical formulation

The primary goal of this work is to achieve the inverse design of tessellated 3D structures. As demonstrated in our previous work (Liu et al., 2020), we can form an axisymmetric morphable 3D structure by connecting several tapered elastic strips through a central hub. In this case, two tapering parameters within each strip should play the role simultaneously to satisfy both the geometric constraint condition of the tessellation and the local bending stiffness matching the desired curvature distribution.

Following the procedure developed in Liu et al. (2020), we determine the relationship between the geometric parameters of the 2D tapered porous sheet (i.e. the perforated kirigami) and the curvature of the 3D desired shape by integrating (6) once,

$$\omega(\xi) \cdot [1 - \varphi(\xi)] = \frac{\tilde{H}(z_* - z) + \tilde{V}(x_* - x)}{\mathrm{d}\theta/\mathrm{d}\xi}. \tag{7}$$

It is clearly seen that there are two tailoring variables, the width profile, $\omega(\xi)$, and the local porosity, $\varphi(\xi)$. Following Liu et al. (2020), we determine the width tapering to satisfy the geometric constraint of tessellation: edges of neighbouring strips touch each other throughout. This means the width profile, $\omega(\xi)$, must be compatible with the deformation in that $\omega(\xi) = (2L/w_0) \cdot x(\xi) \cdot \tan(\pi/N)$, where N is the number of strips we choose to make the morphing structure, and $x(\xi) = 1 + \varepsilon - \tilde{\Delta} - \int_0^\xi \cos\theta(\xi')\, \mathrm{d}\xi'$ is the x-coordinate of a particular element in the deformed configuration,

5

in which, ε is the radius of the central hub, as marked in fig. 2(a). We can therefore determine $\omega(\xi)$, which implicitly contains the local inclination angle, $\theta(\xi)$, as

$$\omega\big[\xi;\theta(\xi)\big] = \frac{2\tan(\pi/N)\cdot L}{w_0}\left[\varepsilon + X(\xi)\right], \tag{8}$$

where $X(\xi) = 1 - \tilde{\Delta} - \int_0^{\xi}\cos\theta(\xi')\,\mathrm{d}\xi'$. Note that this is determined independently of the local porosity; by substituting eq. (8) into eq. (6) (assuming $\varphi(\xi) = 0$) and applying particular boundary conditions, we achieve tessellating 3D axisymmetric shapes. However, the profile of these shapes are not those desired. To match the desired profile, whilst maintaining the tessellation, we tune the distribution of local porosity. Rearranging eq. (7), we relate the local porosity, $\varphi(\xi)$, to the curvature of the desired shape, $\theta(\xi)$, as

$$\varphi(\xi) = 1 - \frac{\tilde{H}(z_* - z) + \tilde{V}(x_* - x)}{\omega(\xi)\cdot\theta_\xi}. \tag{9}$$

For a given desired 3D target structure, once we extracted its curvature distribution, $\theta(\xi)$, as the input information, we can solve eqs. (8) and (9), together with appropriate boundary conditions, to obtain the geometric information of the cut pattern of the 2D flat sheet (both the width, $\omega(\xi)$, and the local porosity distribution, $\varphi(\xi)$).

Here it should be noted that, eq. (8) can be directly solved once we have the curvature information from the target shape. However, to solve eq. (9), we need to determine the unknown parameters, H_0 and z_* (with horizontal load only) or V_0 and x_* (with vertical load only), or all of them together (with both horizontal and vertical loads simultaneously). We take the simplified situation in which the structure is subject only to a horizontal load as an example; then eq. (9) can be reduced to

$$\varphi(\xi) = 1 - \frac{\tilde{H}(z_* - z)}{\omega(\xi)\cdot\theta_\xi}. \tag{10}$$

According to Liu et al. (2020), we can classify two types of situations depending on whether the desired 3D shape has an inflection point, i.e. whether there is any intermediate $\xi_* \in [0,1]$ satisfying $\theta_\xi(\xi_*) = 0$ – the two cases are denoted: (a) no inflection point, and (b) one inflection point. We can summarize the solution of the two unknown parameters (H_0 and z_*) corresponding to the particular boundary conditions, for situation (a)

$$\tilde{H} = \frac{\omega(0)\theta_\xi(0) - \omega(1)\theta_\xi(1)}{y(1)}, \quad z_* = \frac{\omega(0)\theta_\xi(0)}{\tilde{H}}, \tag{11}$$

and, for situation (b)

$$z_* = \int_0^{\xi_*}\sin\theta\,\mathrm{d}\xi, \quad \tilde{H} = \frac{\theta_\xi(0)}{z_*}. \tag{12}$$

Substituting eq. (11) or (12) into eq. (10), together with eq. (8), the inverse design problem is fully solved. Similar results can be obtained for the situation of a vertical load only. It should also be noted that the local porosity must satisfy $\varphi(\xi) \in [0,1]$; to ensure this, we scale the local porosity calculated from eq. (10) as $\bar{\varphi}(\xi) = 1 - [1 - \varphi(\xi)]/\max[1 - \varphi(\xi)]$.

3.2. Demonstration of inverse design strategy

As a first demonstration of the inverse design framework proposed in Section 3.1, we choose a hemisphere as the target 3D structure. This structure can be morphed by applying horizontal loads to a 2D cut sheet with distributed local porosity (i.e. the perforated kirigami). From an expression for the profile of the target structure, most readily the intrinsic equation $\theta(s)$ but equivalently $[x(s), y(s)]$, we design the 2D cut pattern as follows: the distribution of both width, $w(s)$, is calculated numerically from eq. (8) and the expression for $X(\xi)$ following (8), while the local porosity $\varphi(s)$ is calculated from eqs. (10) and (11) (since this target shape is without inflection point). To simplify the fabrication, we consider a narrow rectangular slot with width, h, to represent a row of small pores, similar to the cases shown in fig. fig:fig1(d). Note that, for given distribution of local porosity, the width h is proportional to the global porosity of the cut sheet, ϕ. Here we choose to use eight strips ($N = 8$) to make up the structure. The designed 2D cut pattern is fabricated by laser cutting a uniform square flat sheet with dimensions $\Gamma \times \Gamma \times t$ (with $\Gamma = 189$ mm and $t = 0.3$ mm are the width and thickness of the flat sheet, respectively), and the slot width is set as $h/\Gamma = 0.0096$, see Appendix A.1 for more details. The cut pattern of the flat sheet is shown in fig. 2(a).

To ensure the cut sheet is subject to precise boundary conditions at the distal edge of each strip, we also 3D printed a base with eight grooves that match the width and thickness of the distal edge of each strip (see Appendix A.1 for more details). The position and inclination angle of each groove correspond to the boundary conditions of displacement and rotation angle required for the final shape. Inserting each strip into the groove tightly, we obtain the 3D morphed structure shown in fig. 2(b). We also perform FEM simulations to validate this example of morphing — the morphed shape obtained from FEM is shown in fig. 2(d). The details of FEM simulation are given in Appendix B. From both experiments and simulations, we see clearly that the axisymmetric tessellated 3D structure is obtained.

We also simulate two cases with different slot widths in FEM simulations, comparing to those cases with $h/\Gamma = 0.0096$ shown in figs. 2(b) and (d), namely smaller slot, $h/\Gamma = 0.0048$, and larger slot, $h/\Gamma = 0.0144$; the obtained morphed shapes are shown in figs. 2(c) and (e), respectively. All these cases show the good match with the target shape; this indicates that the value of slot width h (or correspondingly, the global porosity, ϕ) doesn't affect the shape of the morphed structure. The color map of figs. 2(c-e) shows the distribution of strain within the morphed structure; the corresponding maximum values of the strain for (c-e) are $\epsilon_{max} < 0.5\%$. The extremely small strain confirms that the bending-induced deformation is almost isometric and indicate that this kind of design strategy can be easily implemented within a broad range of materials without inducing material failure.

Furthermore, the coordinates of the mid-line profile of the axisymmetric morphed 3D structures (along the yellow line as marked in fig. 2(a)) are extracted from both experiment (the shape in fig. 2(b)) and FEM simulations (figs. 2(c-e)). They are quantitatively compared with the profile predicted by the theoretical model (which is the same as the target shape, by construction) and shown in fig. 2(f). The excellent agreement between theory, experiment and simulations indicates that the inverse design method is effective. It is worth noting that our main goal here is to provide a design strategy to create 3D structures with different apparent shapes. The porosity introduced here is incidental — its role is simply to modify the bending stiffness of the cut sheet locally. The resulting porous structures may be used directly (for example as building facade or packaging) but could also be used as the frame or reinforcement of 3D structures with different shapes by adding

thin, continuous membranes. We shall explore these implications in future work. Now, therefore, we move on to explore the mechanical performance of the morphed 3D structures.

4. Rigidity of Morphed 3D Structures

To create functional and resilient 3D structures via this kind of inverse design strategy, understanding the mechanical characteristics of the morphed structure is essential. Considering the created hemi-spherical morphing structure has the potential for application in various engineering structures, such as infrastructures, we examine its rigidity in indentation as a proxy of its overall load-bearing capacity: how does geometry influence the structural rigidity within the linear elastic regime?

Previous studies indicated that the stiffness of a continuous ellipsoidal shell is strongly dependent on its geometry (Vella et al., 2012a; Lazarus et al., 2012), in which the aspect ratio a/b is an important geometric parameter. As an extension to the hemisphere (with $a/b = 1.0$), we also create several half-ellipsoid morphing structures with aspect ratio a/b in the range $0.5 \leq a/b \leq 2.0$. The experimental and numerical realization of three half-ellipsoids with $a/b = 0.5$, 1.0 and 2.0 are shown in figs. 3(a)-(*i-iii*) and (b)-(*iv-vi*), respectively. Note that these structures are cut from square sheets with the same width, $\Gamma = 189$ mm and with same slot width $h/\Gamma = 0.0096$.

We quantify the structural rigidity of these morphed 3D structures via indentation tests. The test setup is displayed in fig. 3(a)-(*iii*): The top central hub of the morphed structure is indented by a probe (the 'indenter') with a flat tip, to a depth of $D = 10$ mm (see Appendix A.2 for details). The measured relationships between the applied indentation depth, D, and the measured reaction force, F, are presented in fig. 3(c). The initial stiffness of each morphed structure is measured from the $F - D$ curves within the linear elastic regime ($D \lesssim t$, as suggested in (Lazarus et al., 2012)); this defines the (linear) rigidity of the morphed structure. The measured value of K is plotted as a function of a/b in fig. 3(d) by blue circles. We also implement the indentation test in FEM simulations for samples with $a/b = 0.5$, 0.75, 1.0, 1.5, and 2.0, and the numerically measured rigidity are plotted in fig. 3(d) as blue diamonds; experiments and FEM simulations show consistent results here. Interestingly, the relationship between K and a/b is non-monotonic. This non-monotonic relationship is resulting from the complex interplay of geometric and structural factors but can be roughly correlated to the global porosity, ϕ, which determines the weakening effect on the bending stiffness of strips by removing materials. We measure ϕ for morphed structures with different a/b and plot $1-\phi$, which can be referred as the volume fraction of solid, as a function of a/b in fig. 3(d) by red squares. It is clearly seen that there is positive correlation between K and $1 - \phi$.

As already discussed (Section 3.2), the same morphed shape can be realized by using cut patterns with the same distribution of local porosity and changing only the width of each rectangular slot (defined in the top right sub-plot of fig. 2(a), which is also proportional to the global porosity). We therefore perform FEM simulations to investigate the rigidity of these variants on a single morphed structure to quantify the role of slot width (or correspondingly, the global porosity). More specifically, we evaluate the rigidity of structures with $a/b = 0.5$, 1 and 2 for both narrower and wider slots. All the numerically measured values of the rigidity are plotted in fig. 4(a). Comparing to the cases with $h/\Gamma = 0.0096$ (see diamonds), and the same value of a/b, the narrower slot cases ($h/\Gamma = 0.0048$, see lower triangles) are stiffer while the wider slot cases ($h/\Gamma = 0.0144$, see upper triangles) are softer. These findings are in line with expectations: in general, a morphed structure should be stiffer when we remove less material from the sheet (i.e. corresponding to smaller global porosity) with given cut pattern. However, this also provides a new opportunity to tune the rigidity

of a given target structure. From fig. 4(a) we can also notice that, for the cases with given slot width (or global porosity), the non-monotonic trends between K and a/b always hold.

To quantitatively explore the relationship between the rigidity K and the global porosity ϕ, we plot K as a function of $1 - \phi$ for different value of a/b in the insert of fig. 4(b). It is clearly seen the linear correlation between K and $1 - \phi$; that is, for given a/b, the morphed structure with smaller global porosity ϕ corresponds to larger rigidity K. From fig. 4(a) we have seen the rigidity K is depending on the slot width h, equivalently the global porosity ϕ. However, as shown in fig. 4(b), the scaling with porosity can be understood by rescaling K with the global solid fraction $1 - \phi$: since the bending stiffness is proportional to the solid fraction, this rescaling removes the porosity-dependence, with only the aspect-ratio dependence remaining.

The rigidity of continuous ellipsoidal shells is known to depend on the aspect ratio a/b (Vella et al., 2012a; Lazarus et al., 2012). One natural question is that how stiff the morphed shell (which is referred as the tessellated shell) is compared to the continuous shell of the same gross shape. Vella et al. (2012b) showed that the rigidity of a continuous shell with aspect ratio a/b can be calculated as $K_{cont} = 8B/l_b^2$, where $l_b = \sqrt{(pR/Eh)}R$ is the bending length scale calculated with the radius of curvature local to the indentation point, $R = a^2/b$. We can therefore readily calculate the rigidity of continuous shells with different values of a/b when the perimeter is fixed as a constant (which is constrained by the dimension of the flat sheet, Γ). The ratios between the rigidity of tessellated shells (with different slot width h) and continuous shells, K_{tess}/K_{cont}, are plotted as a function of a/b in fig. 3(e). It is clearly seen that the ratio is increasing with the increase of a/b. As might be expected, the rigidity of tessellated shells are much smaller than the corresponding continuous shells in general; we find that $K_{tess}/K_{cont} < 0.05$: since the tessellated shell is comprised of eight separated strips, which are free to separate upon indentation, and therefore the constraint that is an integral part of the geometric rigidity of the continuous shell is easily released. In addition, to match the curvature distribution of the target structure, we introduced porosity into the cut sheet to tailor its bending stiffness (and hence shape), thereby further weakening the stiffness of the morphed structures.

To further explore the difference between the tessellated shell and the continuous shell, we normalize all the results of rigidity obtained from FEM simulations (and calculations) by their value for the equivalent hemisphere ($a/b = 1.0$), i.e., $\bar{K} = K/K_s$ where $K_s = K(a/b = 1.0)$, and show how the normalized rigidity $\bar{K}$ varies with the aspect ratio a/b for both tessellated and continuous shells in fig. 3(f). There are two main important findings: First, the rigidity of tessellated shells with different slot width h are collapsed to a single curve, which indicate that the relationship between K and a/b is only depending on the distribution of the local porosity; Second, different from the tessellated shells having a non-monotonic relationship between $\bar{K}$ and a/b with minimal rigidity at $a/b = 1.0$, the continuous shells have monotonic decreasing $\bar{K}$ as a function of a/b. This difference of the dependence of $\bar{K}$ on a/b can be naturally ascribed to the release of the geometric constraint due to the separation of the strips which form the tessellated shells; we leave a detailed analysis of the deformation mechanism of the tessellated shells for a future study.

5. Discussion and conclusion

In conclusion, this work introduced a general strategy for the inverse design of shape-morphing structures based on kirigami sheets with distributed porosity. The tessellation pattern and the distribution of local porosity can be explicitly predicted by our theoretical model based on a modification of the tapered elastica equation. We validate this theoretical framework through a

detailed demonstration of the inverse design of a hemispherical structure combined with physical experiments and FEM simulations. Note that the design framework is general, regardless of the geometric shape and size of the target shape. We also presented three additional examples to demonstrate the generality of this method, as shown in fig. 5. We can expect that this strategy would be applicable for the design of different kinds of structures, such as shape-adaptive robotics, large-span infrastructures and macro-scale spacecraft structures, with potential applications in a wide range of engineering scenarios.

We also evaluated the load-bearing capacity of morphed half-ellipsoidal structures with different aspect ratios via indentation tests; this revealed an interesting non-monotonic trend of the geometric rigidity with respect to the aspect ratio that has been confirmed by both simulations and experiments. We argued that this non-monotonic trend could be attributed to the interplay of geometric and structural factors and phenomenologically correlated to the global porosity. We hope this preliminary investigation on the mechanical responses of shape-morphing structures will provide guidance for the design of functional and resilient 3D structures via morphing strategy, and furthermore, to motivate more in-depth studies in this area.

Appendix A. Experimental details

Appendix A.1. Fabrication

The 2D sheet with designed pattern is cut from a Mylar film with dimensions of 189 mm × 189 mm × 0.30 mm using a 60 Walt Denford VLS 4.60 laser cutter with the power and speed settings listed in Table A.1.

Table A.1: Parameters are used for laser cutting

Parameters	Power (%)	Speed (%)	PPI (pulses per inch)	Z-axis (mm)
Value	56.1	100	500	0.3

The cut sample is clamped to a solid base designed to impose the given boundary conditions, i.e. the displacement Δ and the inclined angle at the distal edge. The base is 3D printed in hard plastic, namely polylactic acid (PLA, with Young's modulus ≈ 2 GPa). Clamping of each strip is achieved by printing a groove within the base into which additional material at the end of each strip could be inserted, guaranteeing a particular edge inclination angle is achieved.

Appendix A.2. Indentation test

We perform the indentation tests by using an cylindrical indenter made by aluminium alloy with a flat tip. The aluminium indenter ($E \approx 69$ GPa) has one magnitude higher stiffness than the Mylar ($E \approx 1.9$ GPa) sheet. The diameter of the indenter tip is 20 mm, which covers the entire central hub of the morphed structures. The indentation depth of $D = 10$ mm is applied at a rate of 1 mm/min (ensuring that the test is performed quasistatically). The applied force is recorded by an INSTRON testing machine with a 100 N load cell.

Appendix B. FEM Simulations

Computational analyses are performed by using the commercial finite element analysis software (ABAQUS 6.19) to simulate both the shape morphing process and the indentation test. 4-node

shell elements (S4R) were used in every model. The material properties of Mylar are used in all the simulations (i.e. Young's modulus $E = 1.9$ GPa and Poisson s ratio $v = 0.3$). There are two steps set in the FEM simulation: the first step, applying the appropriate boundary conditions (both the displacement and the inclined angle at the distal edge) to achieve the morphed state, and the coordinates of the profile of the morphed structures are measured; the second step, applying the vertical displacement to the central hub of the 3D morphed structure, and record the displacement and reaction force simultaneously.

K. Oliver, A. Seddon, R. S. Trask, Morphing in nature and beyond: a review of natural and synthetic shape-changing materials and mechanisms, Journal of Materials Science 51 (24) (2016) 10663–10689.

C. Huang, Z. Wang, D. Quinn, S. Suresh, K. J. Hsia, Differential growth and shape formation in plant organs, Proceedings of the National Academy of Sciences 115 (49) (2018) 12359–12364.

J. Wang, Q. Zhao, Y. Wang, Q. Zeng, T. Wu, X. Du, Shape-Programmable Electronics: Self-Unfolding Flexible Microelectrode Arrays Based on Shape Memory Polymers, Advanced Materials Technologies 4 (11) (2019) 1970063.

Z. Wang, H. Jiang, G. Wu, Y. Li, T. Zhang, Y. Zhang, X. Wang, Shape-programmable three-dimensional microfluidic structures, ACS Applied Materials & Interfaces 14 (13) (2022) 15599–15607.

G. Z. Lum, Z. Ye, X. Dong, H. Marvi, O. Erin, W. Hu, M. Sitti, Shape-programmable magnetic soft matter, Proceedings of the National Academy of Sciences 113 (41) (2016) E6007–E6015.

K. Liu, F. Hacker, C. Daraio, Robotic surfaces with reversible, spatiotemporal control for shape morphing and object manipulation, Science Robotics 6 (53) (2021a) eabf5116.

L. Wang, D. Zheng, P. Harker, A. B. Patel, C. F. Guo, X. Zhao, Evolutionary design of magnetic soft continuum robots, Proceedings of the National Academy of Sciences 118 (21) (2021) e2021922118.

I. D. McCue, G. M. Valentino, D. B. Trigg, A. M. Lennon, C. E. Hebert, D. P. Seker, S. M. Nimer, J. P. Mastandrea, M. M. Trexler, S. M. Storck, Controlled shape-morphing metallic components for deployable structures, Materials & Design 208 (2021) 109935.

A. Sofla, S. Meguid, K. Tan, W. Yeo, Shape morphing of aircraft wing: Status and challenges, Materials & Design 31 (3) (2010) 1284–1292.

D. Li, S. Zhao, A. Da Ronch, J. Xiang, J. Drofelnik, Y. Li, L. Zhang, Y. Wu, M. Kintscher, H. P. Monner, et al., A review of modelling and analysis of morphing wings, Progress in Aerospace Sciences 100 (2018) 46–62.

E. Siéfert, E. Reyssat, J. Bico, B. Roman, Bio-inspired pneumatic shape-morphing elastomers, Nature Materials 18 (1) (2019) 24–28.

J. W. Boley, W. M. Van Rees, C. Lissandrello, M. N. Horenstein, R. L. Truby, A. Kotikian, J. A. Lewis, L. Mahadevan, Shape-shifting structured lattices via multimaterial 4D printing, Proceedings of the National Academy of Sciences 116 (42) (2019) 20856–20862.

B. Zou, C. Song, Z. He, J. Ju, Encoding of direct 4D printing of isotropic single-material system for double-curvature and multimodal morphing, Extreme Mechanics Letters (2022) 101779.

A. Nojoomi, H. Arslan, K. Lee, K. Yum, Bioinspired 3D structures with programmable morphologies and motions, Nature Communications 9 (1) (2018) 1–11.

B. Yiming, T. Liu, G. Nian, Z. Han, Z. Jia, S. Qu, Mechanics-guided design of shape-morphing composite sheets with hard and soft materials, Extreme Mechanics Letters 35 (2020) 100643.

Y. Tao, Y.-C. Lee, H. Liu, X. Zhang, J. Cui, C. Mondoa, M. Babaei, J. Santillan, G. Wang, D. Luo, et al., Morphing pasta and beyond, Science Advances 7 (19) (2021) eabf4098.

V. Q. Nguyen, A. S. Ahmed, R. V. Ramanujan, Morphing soft magnetic composites, Advanced Materials 24 (30) (2012) 4041–4054.

L. Wang, Y. Kim, C. F. Guo, X. Zhao, Hard-magnetic elastica, Journal of the Mechanics and Physics of Solids 142 (2020) 104045.

A. K. Bastola, M. Hossain, The shape–morphing performance of magnetoactive soft materials, Materials & Design 211 (2021) 110172.

J. Tang, Q. Yin, M. Shi, M. Yang, H. Yang, B. Sun, B. Guo, T. Wang, Programmable shape transformation of 3D printed magnetic hydrogel composite for hyperthermia cancer therapy, Extreme Mechanics Letters 46 (2021) 101305.

M. Liu, L. Domino, D. Vella, Tapered elasticæ as a route for axisymmetric morphing structures, Soft Matter 16 (33) (2020) 7739–7750.

Z. Meng, M. Liu, H. Yan, G. M. Genin, C. Q. Chen, Deployable mechanical metamaterials with multistep programmable transformation, Science Advances 8 (2022) eabn5460.

T. van Manen, S. Janbaz, A. A. Zadpoor, Programming the shape-shifting of flat soft matter, Materials Today 21 (2) (2018) 144–163.

A. Nojoomi, J. Jeon, K. Yum, 2D material programming for 3D shaping, Nature Communications 12 (1) (2021) 1–8.

C. F. Gauss, Disquisitiones generales circa superficies curvas, vol. 1, Typis Dieterichianis, 1828.

M. Liu, L. Domino, I. D. de Dinechin, M. Taffetani, D. Vella, Frustrating frustration in snap-induced morphing, arXiv preprint arXiv:2108.06499 .

A. P. Piedade, 4D printing: the shape-morphing in additive manufacturing, Journal of Functional biomaterials 10 (1) (2019) 9.

D. Vella, Buffering by buckling as a route for elastic deformation, Nature Reviews Physics 1 (7) (2019) 425–436.

R. M. Neville, F. Scarpa, A. Pirrera, Shape morphing Kirigami mechanical metamaterials, Scientific Reports 6 (1) (2016) 1–12.

S. J. Callens, A. A. Zadpoor, From flat sheets to curved geometries: Origami and kirigami approaches, Materials Today 21 (3) (2018) 241–264.

G. Choi, L. H. Dudte, L. Mahadevan, Programming shape using kirigami tessellations, Nature Materials 18 (9) (2019) 999–1004.

A. M. Abdullah, X. Li, P. V. Braun, J. A. Rogers, K. J. Hsia, Kirigami-inspired self-assembly of 3D structures, Advanced Functional Materials 30 (14) (2020) 1909888.

Y. Tang, G. Lin, S. Yang, Y. K. Yi, R. D. Kamien, J. Yin, Programmable kiri-kirigami metamaterials, Advanced Materials 29 (10) (2017) 1604262.

Y. Yang, K. Vella, D. P. Holmes, Grasping with kirigami shells, Science Robotics 6 (54) (2021) eabd6426.

Y. Zhang, F. Zhang, Z. Yan, Q. Ma, X. Li, Y. Huang, J. A. Rogers, Printing, folding and assembly methods for forming 3D mesostructures in advanced materials, Nature Reviews Materials 2 (4) (2017) 1–17.

S. Xu, Z. Yan, K.-I. Jang, W. Huang, H. Fu, J. Kim, Z. Wei, M. Flavin, J. McCracken, R. Wang, et al., Assembly of micro/nanomaterials into complex, three-dimensional architectures by compressive buckling, Science 347 (6218) (2015) 154–159.

Z. Fan, Y. Yang, F. Zhang, Z. Xu, H. Zhao, T. Wang, H. Song, Y. Huang, J. A. Rogers, Y. Zhang, Inverse design strategies for 3D surfaces formed by mechanically guided assembly, Advanced Materials 32 (14) (2020) 1908424.

B. K. Lee, J. F. Wilson, S. J. Oh, Elastica of cantilevered beams with variable cross sections, International Journal of Non-Linear Mechanics 28 (5) (1993) 579–589.

M. A. Isa, I. Lazoglu, Five-axis additive manufacturing of freeform models through buildup of transition layers, Journal of Manufacturing Systems 50 (2019) 69–80.

M. Adnan, A. Abdullah, Z. Samad, Springback behavior of AA6061 with non-uniform thickness section using Taguchi Method, The International Journal of Advanced Manufacturing Technology 89 (5) (2017) 2041–2052.

M. Pezzulla, E. Strong, F. Gallaire, P. Reis, Deformation of porous flexible strip in low and moderate Reynolds number flows, Physical Review Fluids 5 (8) (2020) 084103.

B. Shrimali, M. Pezzulla, S. Poincloux, P. M. Reis, O. Lopez-Pamies, The remarkable bending properties of perforated plates, Journal of the Mechanics and Physics of Solids 154 (2021) 104514.

S. Daynes, P. M. Weaver, Review of shape-morphing automobile structures: concepts and outlook, Proceedings of the Institution of Mechanical Engineers, Part D: Journal of Automobile Engineering 227 (11) (2013) 1603–1622.

L. Kormaníková, E. Kormaníková, D. Katunskỳ, Shape design and analysis of adaptive structures, Procedia Engineering 190 (2017) 7–14.

C. A. Stuart, Buckling of a tapered elastica, C. R. Acad. Sci. I 331 (2000) 417–421.

D. Vella, A. Ajdari, A. Vaziri, A. Boudaoud, Indentation of ellipsoidal and cylindrical elastic shells, Physical Review Letters 109 (14) (2012a) 144302.

A. Lazarus, H. Florijn, P. M. Reis, Geometry-induced rigidity in nonspherical pressurized elastic shells, Physical Review Letters 109 (14) (2012) 144301.

D. Vella, A. Ajdari, A. Vaziri, A. Boudaoud, The indentation of pressurized elastic shells: from polymeric capsules to yeast cells, Journal of the Royal Society Interface 9 (68) (2012b) 448–455.
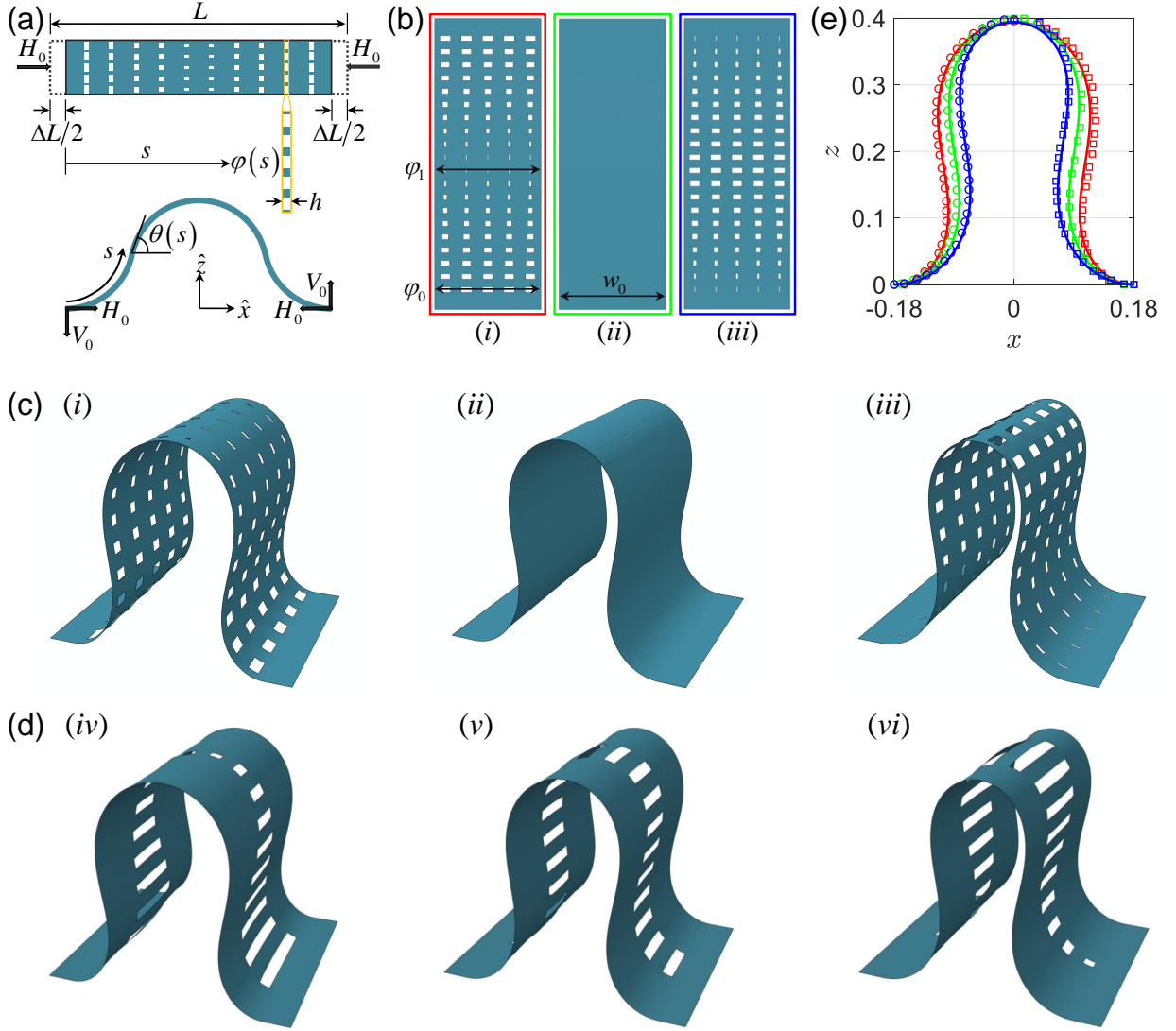
Figure 1: Porous elastic strips with distributed local porosity and their deformation subject to external load. (a) Schematic of a porous strip with distributed local porosity $\varphi(s)$ subject to a horizontal compressive load, H_0. The buckled shape is described by the intrinsic equation $\theta(s)$. (b) Representation of three strips with different local porosity distributions ($\varphi(s)$) but uniform width (w_0) and thickness (t_0); the local porosity ratio between the edge and centre varies in each case as follows: (i) $\varphi_0/\varphi_1 = 10$, (ii) $\varphi_0/\varphi_1 = 1$, (iii) $\varphi_0/\varphi_1 = 0.1$. (c) The deformed shapes obtained from FEA simulations of those three porous strips displayed in (b). (d) The deformed shapes obtained from FEA simulations of three porous strips with same distributions of the local porosity corresponding to (c) but replacing a row of small pores with a single narrow, rectangular slot. (e) Nondimensional buckled shapes of the three porous elastic strips subject to relative end-end compression $\Delta L/L = 0.64$ and clamped boundary conditions, where theoretical predictions from eq. (6) are shown by the solid lines, together with FEM results for strips shown in (c) (circles, left-hand side) and the strips shown in (d) (squares, right-hand side).
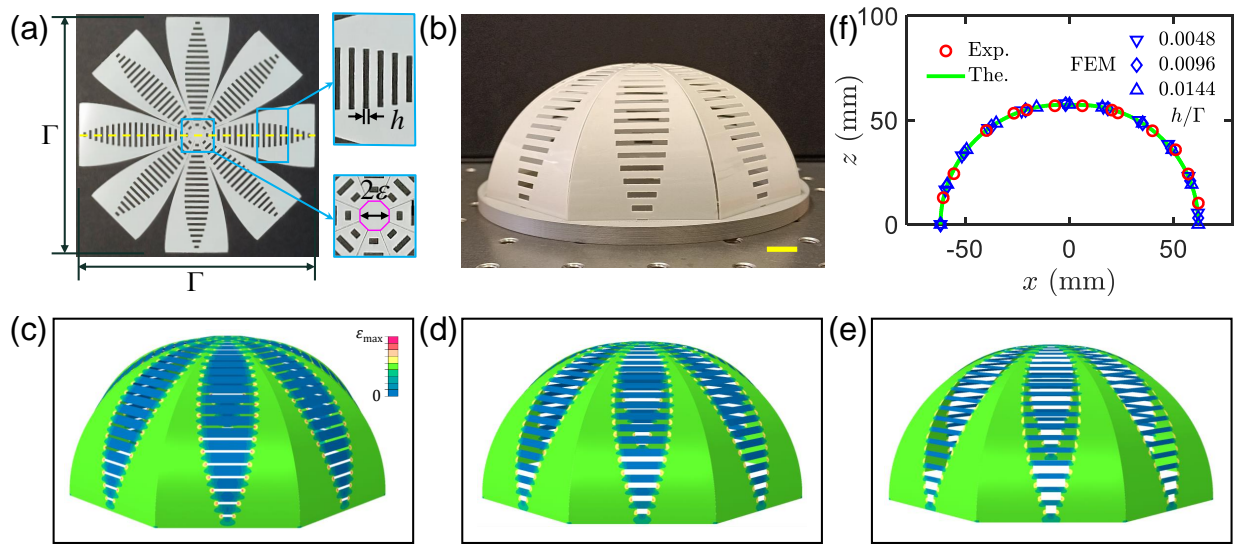
13

Figure 2: Inverse design demonstration of a morphing to a hemisphere in FE simulations and experiment. (a) The cut patterns of the 2D flat sheet predicted by theory to generate the 3D hemisphere. (b) A morphed hemisphere with dimensionless slot width $h/\Gamma = 0.0096$ obtained in physical experiment. (The scale bar represents 1 cm.) (c-e) The 3D morphed hemispheres obtained in FEM simulations with dimensionless slot width: (c) $h/\Gamma = 0.0048$, (d) $h/\Gamma = 0.0096$ and (e) $h/\Gamma = 0.0144$. (f) Comparison of the profiles of the 3D morphed hemispheres obtained from the theory (solid line), experiment (red symbols) and FEM simulations (blue symbols).
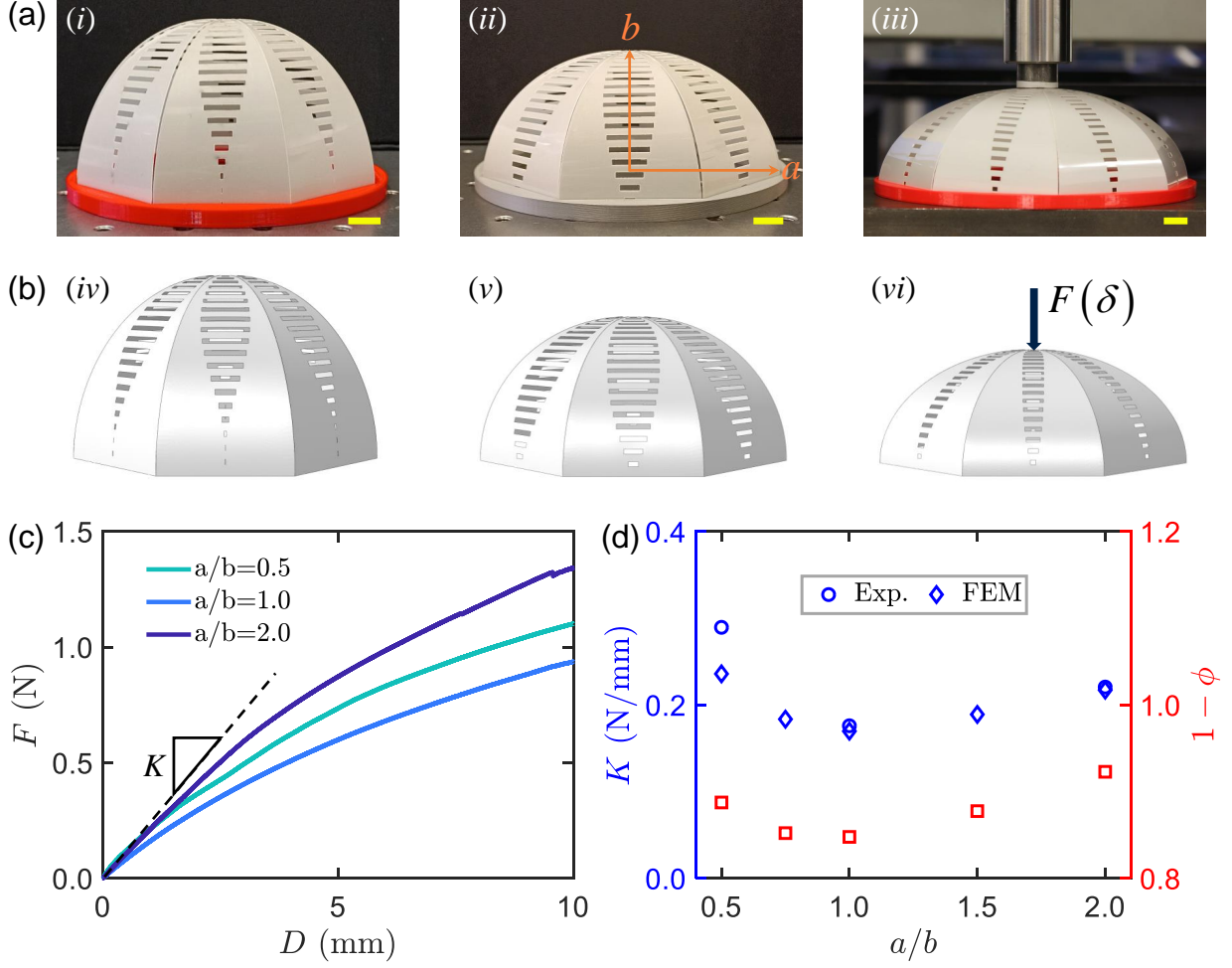
14

Figure 3: Experimental and numerical realization of half-ellipsoids with different aspect ratio and their rigidity measured in indentation tests. (a) The morphed half-ellipsoids obtained in physical experiments with (i) $a/b = 0.5$, (ii) $a/b = 1.0$ and (iii) $a/b = 2.0$. (The scale bars represent 1 cm.) (b) The morphed half-ellipsoids obtained in FEM simulations, the shapes in $(iv\text{-}vi)$ correspond to the physical models in $(i\text{-}iii)$. (c) The force-displacement relationship of half-ellipsoids in indentation tests. (d) The rigidity of the half-ellipsoids measured from both experiments (blue circles) and FEM simulations (blue diamonds) and the corresponding solid volume fractions (red squares) of those half-ellipsoids as a function of aspect ratio
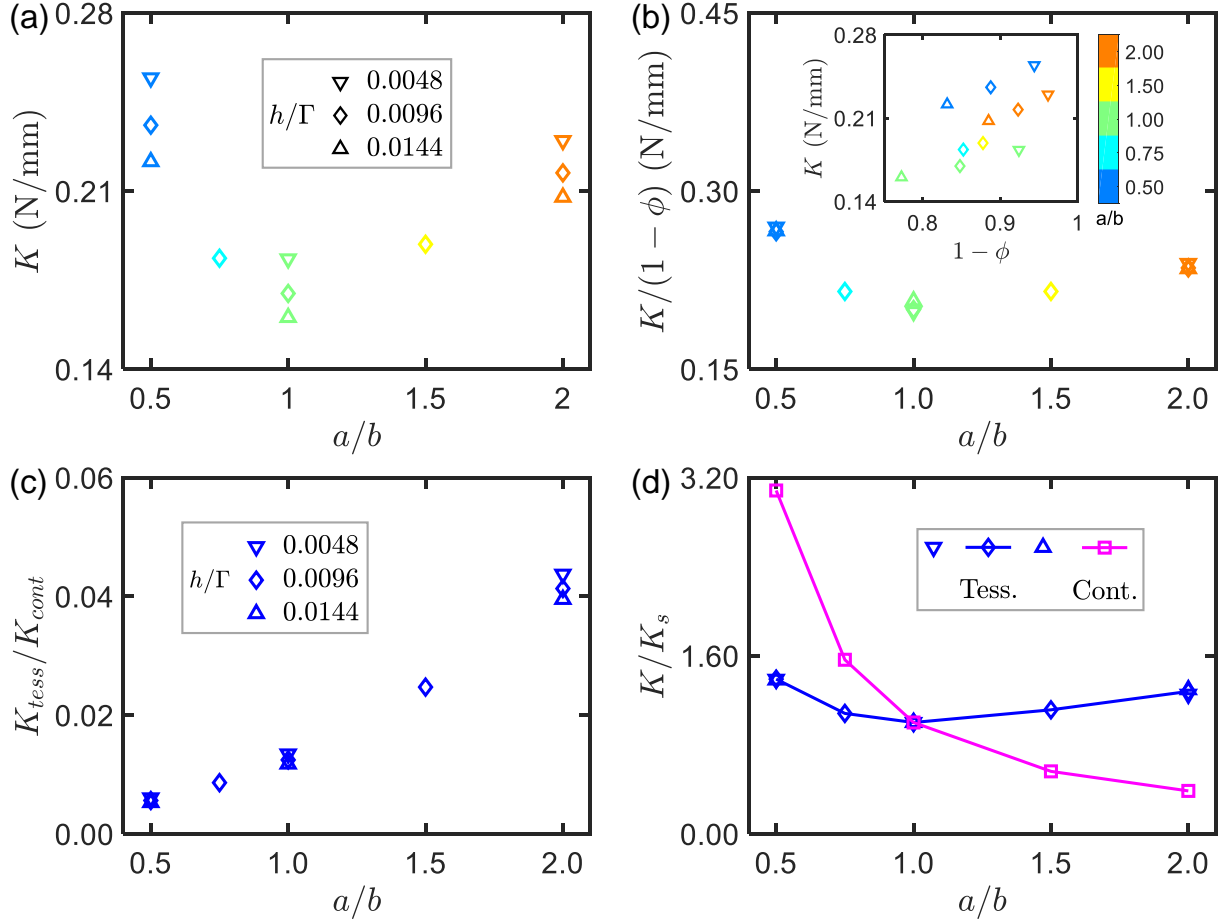
.

Figure 4: The relationship between the rigidity and the aspect ratio of half-ellipsoids. (a) FEM results for the rigidity of half-ellipsoids with three dimensionless slot widths: $h/\Gamma = 0.0048$ (lower triangles), 0.0096 (diamonds) and 0.0144 (upper triangles), where h and Γ are defined in fig. 2(a). (b) The rigidity of half-ellipsoids is normalized by their corresponding solid volume fraction. Insert: The relationship between rigidity solid volume fraction and for different aspect ratios. (c) The rigidity ratio between the morphed structures (referred to as the tessellated shells) and continuous shells with the same aspect ratio. (d) The rigidity of both tessellated shells (blue symbols) and continuous shells (magenta symbols) normalized by the results for the corresponding hemispheres (with $a/b = 1.0$).
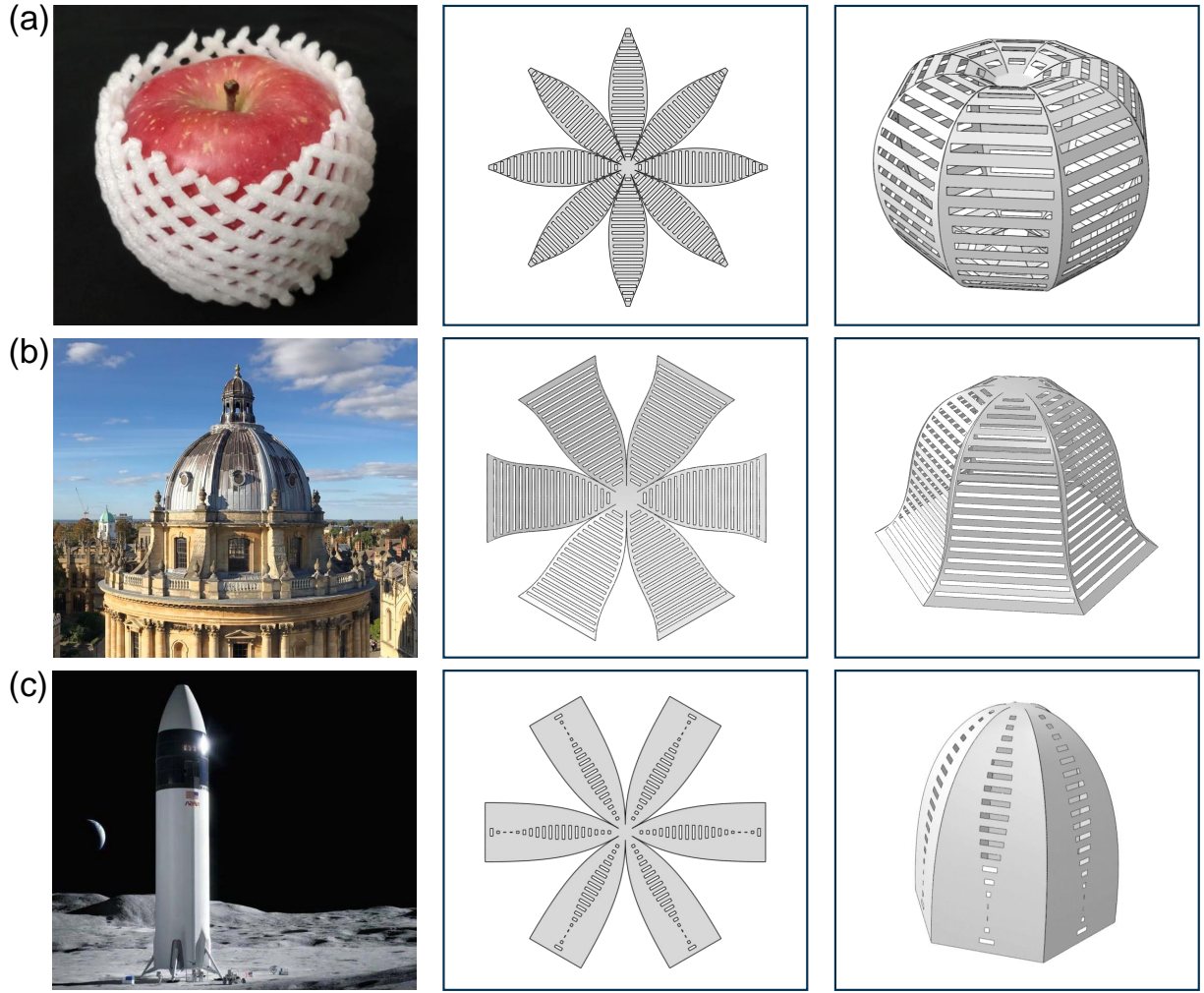
Figure 5: Additional examples of the shape-morphing structures with different shapes based on the inverse design framework. (a) An apple shape structure as a possible gripper or fitted packaging for a real apple. (b) A roof structure with respect to the cupola of the Bodleian Library at the University of Oxford. (c) A cone structure as a possible rocket nose cone (https://www.nasa.gov/). The first column shows the 3D structures with different shapes followed by the 2D cut sheets (perforated kirigami) designed by the theoretical model (second column) and the corresponding morphed 3D structures (third column).